

## Three-dimensional van der Waals Open Frameworks

Shun Tokuda<sup>1,2\*</sup> and Shuhei Furukawa<sup>1,2\*</sup>

<sup>1</sup>Institute for Integrated Cell-Material Sciences (WPI-iCeMS), Kyoto University, Yoshida, Sakyo-ku, Kyoto 606-8501, Japan

<sup>2</sup>Department of Synthetic Chemistry and Biological Chemistry, Graduate School of Engineering, Kyoto University, Katsura, Nishikyo-ku, Kyoto 615-8510, Japan

\*To whom correspondence should be addressed: [shuhei.furukawa@icems.kyoto-u.ac.jp](mailto:shuhei.furukawa@icems.kyoto-u.ac.jp), [tokuda.shun.38n@st.kyoto-u.ac.jp](mailto:tokuda.shun.38n@st.kyoto-u.ac.jp)

**Open framework materials are constructed by connecting molecular components via strong bonds. Here, we show van der Waals interaction, which has been believed to be too weak for the framework construction, joints molecular building blocks into a series of robust three-dimensional frameworks, so-called van der Waals frameworks (WaaFs). The success relies on the use of metal-organic polyhedra (MOPs) with a size over 2 nm as building blocks. The well-defined faces composed of large aromatic molecules increase the intermolecular contact area to gain interaction energy over 400 kJ/mol. The octahedral shape of MOPs directs their packing into a diamond network with large extrinsic porosity. We confirm that one of the WaaFs shows over 2,000 m<sup>2</sup> g<sup>-1</sup> specific surface area.**

Johannes Diderik van der Waals hypothesized an attractive interaction among gas molecules to explain their gas-to-liquid condensation (1). This non-directional interaction, now known as van der Waals interaction, is not limited to gases but ubiquitously found in molecular assemblies. Among chemical forces, van der Waals interaction plays a significant role in many dynamic phenomena, from the physisorption of small molecules on solid surfaces to protein folding because of its weak force and high lability (2, 3). Geckos betray this consensus as they cling to a vertical wall with their adhesive feet, at which thousands of spatulas with a size of around 200 nm collectively interact with the wall surface through van der Waals interaction (4). The key to this performance is that the force of van der Waals interaction depends on the size of the contact area. Here we apply this principle to design an open framework material.

Open framework materials, including metal-organic frameworks (MOFs) and covalent organic frameworks (COFs), are assembled from molecular building blocks via strong bonds (Fig. 1) (5). This is because retaining open voids in their structures as permanent porosity requires the robustness of frameworks. The force of van der Waals interaction is believed to be too weak and irrelevant for the framework construction. This myth must be correct when considering conventional molecular building blocks for constructing MOFs and COFs; a well-known  $\pi$ - $\pi$  stacking interaction is estimated to be less than a few tens kJ/mol (6), which is far weaker than the typical metal-carboxylate bonds found in MOFs (7).

Here we show a strategy of using large supramolecular building blocks with a flat molecular surface to increase the contact area between building blocks and construct a series of open frameworks via van der Waals interaction. We design octahedral metal-organic

polyhedra (MOPs) with over 2 nm of diameter, from which more than 200 atoms collectively form a strong and directional intermolecular interaction at the interface between two MOPs. The assembly of these MOPs directs the formation of diamond-like three-dimensional van der Waals open frameworks with high thermal stability over 300 °C. Thanks to the contributions from the sparse MOP packing and the MOP internal cavity, one of the frameworks shows high permanent porosity over 2,000 m<sup>2</sup> g<sup>-1</sup> specific surface area.

**[INSERT FIGURE 1]**

### **Octahedral metal-organic polyhedra as supramolecular building blocks**

A large contact area between building blocks is the prerequisite for constructing open frameworks via van der Waals interaction. Here we suggest a supramolecular building block approach, in which many molecular components can be pre-assembled to form a large molecular entity with a designable surface structure directed outward. This designability allows for enlarging the contact surface to produce effective interaction between building blocks. Besides the large contact area, supramolecular building blocks must be sparsely packed to avoid their close packing and maintain the open void. Thus, we particularly use MOPs, assembled from organic molecules and metal clusters, whose well-defined polyhedral shapes drive a specific framework topology via polyhedral tessellation through face-to-face interaction. We target a framework with the diamond topology (**dia**) due to its low packing density and the accessibility from highly symmetric tetrahedral connectivity ( $\delta$ ).

When one can design a tetrahedral connectivity from regular polyhedra, there are only two choices either a tetrahedron or an octahedron; both have faces at the tetrahedral positions

available for face-to-face interaction. Tetrahedra tends to pack into a dense diamond arrangement, which is not suitable for an open framework (9). Thus, we selected an octahedral MOP family of  $[M_{12}(NDI_{XX})_{12}]$  ( $M$  = metal ions,  $NDI_{XX}$  = naphthalenediimide (NDI)-based dicarboxylates), in which fourfold symmetric dinuclear paddlewheel motifs of  $[M_2(O_2CR)_4]$  are located at the six vertices of octahedron and they are linked by twelve  $NDI_{XX}$  molecules as the edges (10, 11). One characteristic feature of this MOP family is the versatility of  $NDI_{XX}$ , which is synthesized by the condensation reaction between 1,4,5,8-naphthalenetetracarboxylic dianhydride and  $\alpha$ -amino acid (X) and thus the amino acid residues can be immobilized as functional groups on the main NDI-based dicarboxylic acid backbone. As a consequence, each triangular face of these MOPs is composed of three large and flat NDI moieties surrounded by the corresponding amino acid residues.

We target the Rh(II)-based MOPs because of their known high structural integrity and chemical stability (12). After the screening of different amino acid residues, we synthesized the MOP based on L-phenylalanine (F) with a composition of  $[Rh_{12}(NDI_{FF})_{12}(L)_{12}]$  ( $L$  = solvent molecules coordinating on the axial sites of dirhodium paddlewheels) as amorphous solid by reacting dirhodium(II) tetraacetate with  $NDI_{FF}$  in *N,N*-dimethylacetamide (DMA) (Fig.2A). Rhombic plate-like crystals of the MOP were harvested by the slow vapor diffusion of ethanol into DMA/pyridine mixed solvent solution of the MOP. Single crystal X-ray diffraction (SC-XRD) measurement revealed the formation of the octahedral MOP structure with eight triangular faces, each of which is composed of three NDI moieties and three benzyl groups from phenylalanine (Fig. S1A). However, the MOPs do not strongly interact with each other through these triangular faces in this packing. The interdigitated arrangement of

the benzyl groups from phenylalanine and disordered crystal solvents leads to the distorted face-centered cubic packing (**fcu** net topology) of the MOPs with the orthorhombic  $P2_12_12_1$  space group (Fig. S1B). This packing structure was fragile and readily collapsed by the evaporation of solvent, resulting in the amorphous solids (Fig. S2).

[INSERT FIGURE 2]

### Assembly of MOPs into an open framework

In general, the packing of molecules is highly solvent-dependent, known as pseudo-polymorphism (13). To seek the effective interaction and packing of  $[\text{Rh}_{12}(\text{NDI}_{\text{FF}})_{12}(\text{L})_{12}]$ , we carried out solvent screening and found a very specific condition led to the formation of crystals with a regular octahedral morphology; the best solvent condition was optimized to be the mixed solvent of DMA/ethanol (1/2 volume ratio) with 0.7vol% of pyridine. Note that the rhombic plate-like crystals were harvested at a higher DMA/ethanol ratio (Fig. S3).

The SC-XRD experiments on the octahedral crystal revealed that the  $[\text{Rh}_{12}(\text{NDI}_{\text{FF}})_{12}(\text{L})_{12}]$  crystallizes in the cubic  $F4_132$  space group, in which all six outer axial sites of dirhodium paddlewheels of the octahedral MOP are occupied by pyridine molecules. The MOP is surrounded by four neighboring MOPs via four out of eight triangle faces located at the tetrahedral positions (Fig. 2, B and C). This tetrahedral arrangement of MOPs spans the space and leads to the diamond-like network (**dia** net topology) (Fig. 2, D and E). Thanks to the sparse packing, a large external void space is created in the **dia** network and the external void fraction was estimated to be 35% by the MoloVol program (14) (Fig. 2, F and G; see

the supplementary materials for the calculation detail). This value is twice larger than the contribution from the internal MOP cavity (15 %). Thermogravimetric analysis (TGA) and variable temperature powder X-ray diffraction (VT-PXRD) unveiled the exceptional thermal stability of this packing; TGA determined the thermal decomposition temperature to be 320 °C (Fig. S4) and VT-PXRD confirmed the maintenance of the **dia** network until the thermal decomposition of the MOPs (Fig. 2J). This high stability was also manifested at the single-crystal level; we successfully desolvated submillimeter-sized single crystals by evaporating solvent molecules at 80 °C in the air and confirmed no obvious cracks and maintained transparency (Fig. 2, H and I). Note that the color of the crystal changed from red to grayish blue upon desolvation, which is consistent with the characteristic ligand field effects of the dirhodium paddlewheels (see materials and methods and Fig. S5). This color change was reversibly triggered by switching the humidity of environment, and the color change can be repeated more than 10 times without having noticeable damage on the crystallinity. The integrity of the **dia** network after the multiple cycles of color change was confirmed by the SC-XRD measurement of the dried single crystal (Fig. S6).

Nitrogen sorption experiments at 77 K on the octahedral crystals demonstrated the type-I isotherm with the saturation of gas uptake of 362 cm<sup>3</sup> g<sup>-1</sup> at  $P/P_0 = 0.2$  (Fig. 2K). This uptake capacity is twice larger than that for the amorphous solid of [Rh<sub>12</sub>(NDI<sub>FF</sub>)<sub>12</sub>(L)<sub>12</sub>] building blocks (139 cm<sup>3</sup> g<sup>-1</sup> at  $P/P_0 = 0.2$ ), which confirms the contribution of the stable external voids in the **dia** network for the permanent microporosity. The Brunauer-Emmett-Teller (BET) surface area of the **dia** network was determined to be 1463 m<sup>2</sup> g<sup>-1</sup> from the isotherm by the BETSI program (Fig. S7) (15). This value surpasses the highest value

recorded in the MOP materials ( $1321 \text{ m}^2 \text{ g}^{-1}$ ) (16). The thermal stability, crystallinity, and permanent porosity discovered in the **dia** network satisfy the criteria as a new framework material, similar to MOFs and COFs. Considering that the MOP building blocks are not interconnected by either coordination or covalent bonds but rather simply assembled by non-covalent intermolecular interaction, hereafter we named this **dia**-networked material as van der Waals framework-1 (**WaaF-1**).

To understand the origin of strong intermolecular interactions between the MOPs in **WaaF-1**, we first examined the intermolecular contact from the crystal structure. As shown in Fig. 3A, the MOP-MOP contact can be interpreted as a face-to-face stacking between two triangular faces. Three  $\text{NDI}_{\text{FF}}$  ligands from each face contribute to a tight MOP-MOP contact; six contacting pairs of NDI-NDI were observed with the shortest proximity of  $\text{C}\cdots\text{O}$  ( $3.17(1) \text{ \AA}$ ) that are shorter than the sum of van der Waals radii ( $3.29 \text{ \AA}$ ) and six stacking pairs between a NDI plane from one face and a phenyl ring of  $\text{NDI}_{\text{FF}}$  from the other face were also detected with the average proximity of  $3.48 \text{ \AA}$ . Overall, more than 200 atoms are involved in the intermolecular contact between two faces. No hydrogen bond or specific dominant interaction was observed and the Hirshfeld surface analysis supported the homogeneous contribution of those atoms to the intermolecular contact (Fig. S8). To further evaluate the energetic contributions from different interaction mechanisms, we carried out the energy decomposition analysis (EDA) based on density functional theory (DFT) calculations (17, 18). The energy calculation based on the crystal structure of **WaaF-1** clarified that a pair of triangular faces is stabilized by the overall  $433 \text{ kJ/mol}$  of interaction energy, in which 87% of the stabilization was accounted by London dispersion forces rather than the other

interaction mechanisms including electrostatic (12%) and induction (1%) forces (Fig. 3B, see materials and method for the detail of calculation).

### [INSERT FIGURE 3]

When considering the total number of edges in an octahedron to be twelve, in which three edges (NDI molecules) of the triangle face participate in the face-to-face interaction, four triangles from the octahedron become the interaction faces. Because these triangles cannot share the edges, four triangles must be located at the tetrahedral position. This geometric restriction leads to the formation of a **dia** network in **WaaF-1**.

### Assembly of analogous van der Waals frameworks

A main characteristic feature of open framework materials is isoreticular design, which allows the change of chemical features while maintaining the framework topology. In the case of **WaaF-1**, the large contact area between the triangular faces is mandatory to maintain the **dia** topology. One possible variable structural parameter is one amino acid residue in  $\text{NDI}_{\text{FF}}$  because only one out of two phenyl rings from  $\text{NDI}_{\text{FF}}$  contributes to the NDI-phenyl stacking pair. This fact encouraged us to synthesize the asymmetric NDI ligand with phenylalanine and alanine residues,  $\text{NDI}_{\text{AF}}$  (Fig. 4A, Fig. S9).

### [INSERT FIGURE 4]

The corresponding octahedral building block  $[\text{Rh}_{12}(\text{NDI}_{\text{AF}})_{12}(\text{L})_{12}]$  was synthesized by the same protocol as  $[\text{Rh}_{12}(\text{NDI}_{\text{FF}})_{12}(\text{L})_{12}]$ . The green single crystals with octahedral morphology were harvested by the vapor diffusion of ethanol into the DMA solution of

[Rh<sub>12</sub>(NDI<sub>AF</sub>)<sub>12</sub>(L)<sub>12</sub>]. SC-XRD experiments confirmed that [Rh<sub>12</sub>(NDI<sub>AF</sub>)<sub>12</sub>(L)<sub>12</sub>] crystallizes in the cubic *F*4<sub>1</sub>32 space group, in which the MOP forms the isorecticular **dia** network (Fig. 4B, hereafter **WaaF-2**). The whole structure of **WaaF-2** is almost the same as **WaaF-1** except for two features: solvent molecules of DMA or ethanol coordinate to the axial sites of dirhodium paddlewheels because of the absence of pyridine in the solvents (Fig. S10) and the occupancy of phenyl ring stacking on NDI is refined to be 0.62 rather than the unity. The latter corresponds to the fact that the orientation of NDI<sub>AF</sub> ligand within the MOP is highly scrambled and the observed structure is crystallographically averaged. The ligand scrambling leads to the weakening of the MOP-MOP interaction because the number of contributing NDI-phenyl stacking pairs can be reduced from six in **WaaF-1** to three (averaged) in **WaaF-2**. We estimated the interaction energy between two neighboring MOPs in **WaaF-2** to be 298 kJ/mol of stabilization (Fig. S11), which is lower than the case of **WaaF-1** but still significantly strong to maintain the whole framework.

The octahedral MOPs can be synthesized with Cu(II) ions instead of Rh(II) ions. Indeed, five MOP analogues based on dicopper paddlewheels were reported in the literature (10, 11); however, none of the MOPs were packed in the **dia** network. Though we carried out the screening of crystallization conditions with [Cu<sub>12</sub>(NDI<sub>FF</sub>)<sub>12</sub>(L)<sub>2</sub>] building blocks according to the **WaaF-1** protocol, the characteristic octahedral single crystals were not obtained. We then tried the synthesis of a Cu(II)-based analogue of **WaaF-2**; the solvothermal reaction of asymmetric NDI<sub>AF</sub> ligand with copper(II) nitrate in *N,N*-dimethylformamide (DMF)/ethanol mixed solvent yielded blue single crystals with octahedral morphology. SC-XRD revealed that [Cu<sub>12</sub>(NDI<sub>AF</sub>)<sub>12</sub>(L)<sub>2</sub>] crystallizes in *F*4<sub>1</sub>32 and possesses the isostructural **dia** network

(Fig. 4C, **WaaF-3**). Similar to **WaaF-2**, the NDI<sub>AF</sub> ligands are scrambled with the MOP and the corresponding occupancy of NDI-stacked phenyl ring was refined to be 0.42.

The scrambling of asymmetric ligands over the MOP should be key for the successful formation of the **dia** network. When considering the positions of amino acid residues in the [Cu<sub>12</sub>(NDI<sub>AF</sub>)<sub>12</sub>(L)<sub>2</sub>], half of the 24 locations are occupied by benzyl groups from phenylalanine and the other half by methyl groups from alanine. This consideration motivated us to synthesize another scrambling structure by mixing two ligands within the MOP; scrambling of phenylalanine-based NDI<sub>FF</sub> ligand and alanine-based NDI<sub>AA</sub> ligand should also provide random arrangement of benzyl and methyl groups. Solvothermal reaction of the mixed ligand of NDI<sub>FF</sub> and NDI<sub>AA</sub> in the 1:1 ratio with copper(II) nitrate in DMF/ethanol solvents produced blue octahedral single crystals. This compound crystallizes in *F*<sub>4</sub>32 and showed the isostructural **dia** network (Fig.4D, **WaaF-4**). Two ligands are highly scrambled with the occupancy of phenyl ring as 0.54. <sup>1</sup>H nuclear magnetic resonance (NMR) spectroscopy for the acid-digested crystals revealed the overall ratio of NDI<sub>FF</sub>:NDI<sub>AA</sub> to be 0.48:0.52 (Fig. S12). Considering the similar chemical structures of NDI<sub>FF</sub> and NDI<sub>AA</sub> and the composition of the MOP molecule, the reaction should yield possible 13 chemical compositions of [Cu<sub>12</sub>(NDI<sub>AA</sub>)<sub>x</sub>(NDI<sub>FF</sub>)<sub>12-x</sub>(L)<sub>12</sub>] (*x* = 0, 1, ..., 12) with the stochastic distribution. Mass spectroscopy experiments on the collected single crystals visualized such chemical diversity of **WaaF-4**, by contrast to the case for **WaaF-3** with a single composition (Fig. 4E, S13, and S14).

All **WaaF-2**, **3**, and **4** maintained the crystallinity even after the guest exchange with methanol and the following guest removal as well as showing the similar thermal stability to

**WaaF-1** (Fig. S15–S20). The nitrogen and carbon dioxide gas sorption isotherms of **WaaF-2**, **3**, and **4** showed larger uptakes than **WaaF-1** because of the absence of pyridine molecules at the axial site (Fig. 4F, S21). Indeed, the diameter of extrinsic voids was enlarged from 16 Å for **WaaF-1** to 23 Å for **WaaF-2** (Fig. S22). The BET surface areas were determined to be 1870, 2075, and 1992 m<sup>2</sup>g<sup>-1</sup>, and the pore volumes were estimated to be 0.80, 0.88, and 0.84 cm<sup>3</sup>g<sup>-1</sup> for **WaaF-2**, **3**, and **4**, respectively (Fig. S23–S25). These values overshoot the previous record of **WaaF-1** (BET surface area = 1463 m<sup>2</sup>g<sup>-1</sup>, pore volume = 0.60 cm<sup>3</sup>g<sup>-1</sup>).

## Discussions

The design principle of WaaFs is how to resist a general habit of molecular crystallization that tends to closely pack to maximize the intermolecular interaction (19). By contrast to the cases of MOFs, COFs, or hydrogen-bonded organic frameworks (HOFs), which use directional strong bonds, defining the interaction direction by molecular packing via van der Waals interactions is difficult. To date, several molecular systems have been serendipitously discovered to generate extrinsic microporosity by molecular packing (20-26); however, a design principle to construct a series of frameworks has not been generalized. This is because each system relies on a specific molecular shape, and the tiny modification of the molecular structure can drive a significant change in packing, leading to the diminishing of the extrinsic porosity. In this study, the series of WaaFs was constructed based on the same structural motif with a large contact area that forms a strong van der Waals “bond” (Fig. 5). The

modularity of MOP building blocks allows for introducing different metal ions and functional groups while maintaining the structural scaffold of the framework.

**[INSERT FIGURE 5]**

To generate extrinsic porosity, molecular building blocks must be strongly packed while trapping solvent molecules that, in turn, can be removed without disturbing the packing structure. Recent studies on porous molecular crystals demonstrated that the weakening of the interaction between solvents and building blocks is crucial to strengthening the interactions between building blocks (27). The results of solvent screening to discover **WaaF-1** follow this principle. In general, the  $[\text{Rh}_{12}(\text{NDI}_{\text{FF}})_{12}(\text{L})_{12}]$  molecule is well dissolved in DMA, and the crystallization process is highly dependent on the counter solvent. While the non-porous **fcu** packing was formed with the low fraction of ethanol in DMA, the increase of ethanol ratio over ethanol/DMA = 2/1 selectively produced the porous **dia** network. This is most likely because ethanol-rich mixed solvents weakly interact with MOPs and the MOP-MOP interaction takes a major role during the crystallization process. The solvents possessing similarly weaker dispersion interaction, such as methanol or acetonitrile, can be alternatively used instead of ethanol to form the **dia** network (Fig. S26, S27).

The chemical stability of **WaaF-1** also follows a similar solvent-dependency; while solvents with strong dispersion interaction, such as chloroform, tetrahydrofuran, and 1,4-dioxane, dissolve **WaaF-1** into the MOP solution, the crystallinity was maintained after immersing in methanol, ethanol, or even after boiling in water for more than 3 days at 100 °C (Fig. S28). The solvent-specific stability of **WaaF-1** coincides with the general character

of van der Waals interactions and suggests the high potential of WaaFs for their solution processability and facile structural regeneration by recrystallization.

Besides gaining intermolecular contact area, the polyhedral structural design of molecular building blocks has two crucial features for constructing WaaFs. First, the arrangement of molecular components to form a hollow polyhedron generates the internal cavity. This feature creates the hierarchical porosities together with the larger extrinsic void in WaaFs (Fig. S29). As is observed in the rapid color change in **WaaF-1** single crystals in response to humidity, this characteristic pore structure provides the fast diffusion of water molecules through the extrinsic pore and the adsorption of water on the open metal sites of dirhodium paddlewheels located inside the MOP cavity.

The second important feature is the controllable directionality of the van der Waals bonds. As the series of WaaFs demonstrated the stacking of octahedral MOPs to form **dia** network by repeating tetrahedral arrangement, the polyhedral shape defines the relative arrangement of the neighboring molecules. In other words, the different polyhedral shapes of MOPs could lead to their assembly into a different topology of open frameworks. This structural control can be understood as polyhedral tiling in three-dimensional space. Because not a few network topologies of MOFs have been discovered based on the polyhedral tiling (28–30), there is a profound chemical space of WaaFs that can be targeted by a rational design of MOPs. The ubiquity of van der Waals interaction implies this material discovery is possible by any class of organic, inorganic, or organic-inorganic hybrid materials with well-defined polyhedral shapes.

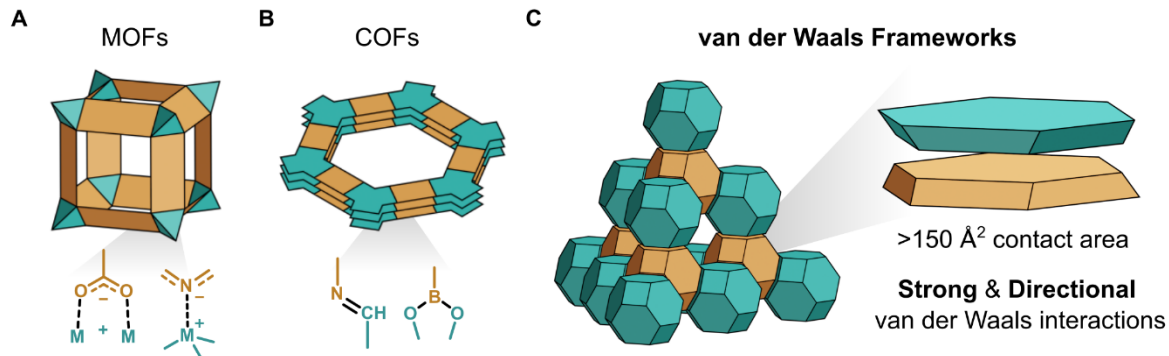


**Fig. 1: Category of open framework materials.** Schematic illustrations and representative strong bond motifs of (A) metal-organic frameworks (MOFs), (B) covalent organic frameworks (COFs), and (C) van der Waals frameworks (WaaFs). By contrast to the strong bonds in MOFs and COFs are typically composed of a few atoms, a linkage of molecular building blocks in WaaFs is based on a large intermolecular contact, which generates strong and directional van der Waals interactions.

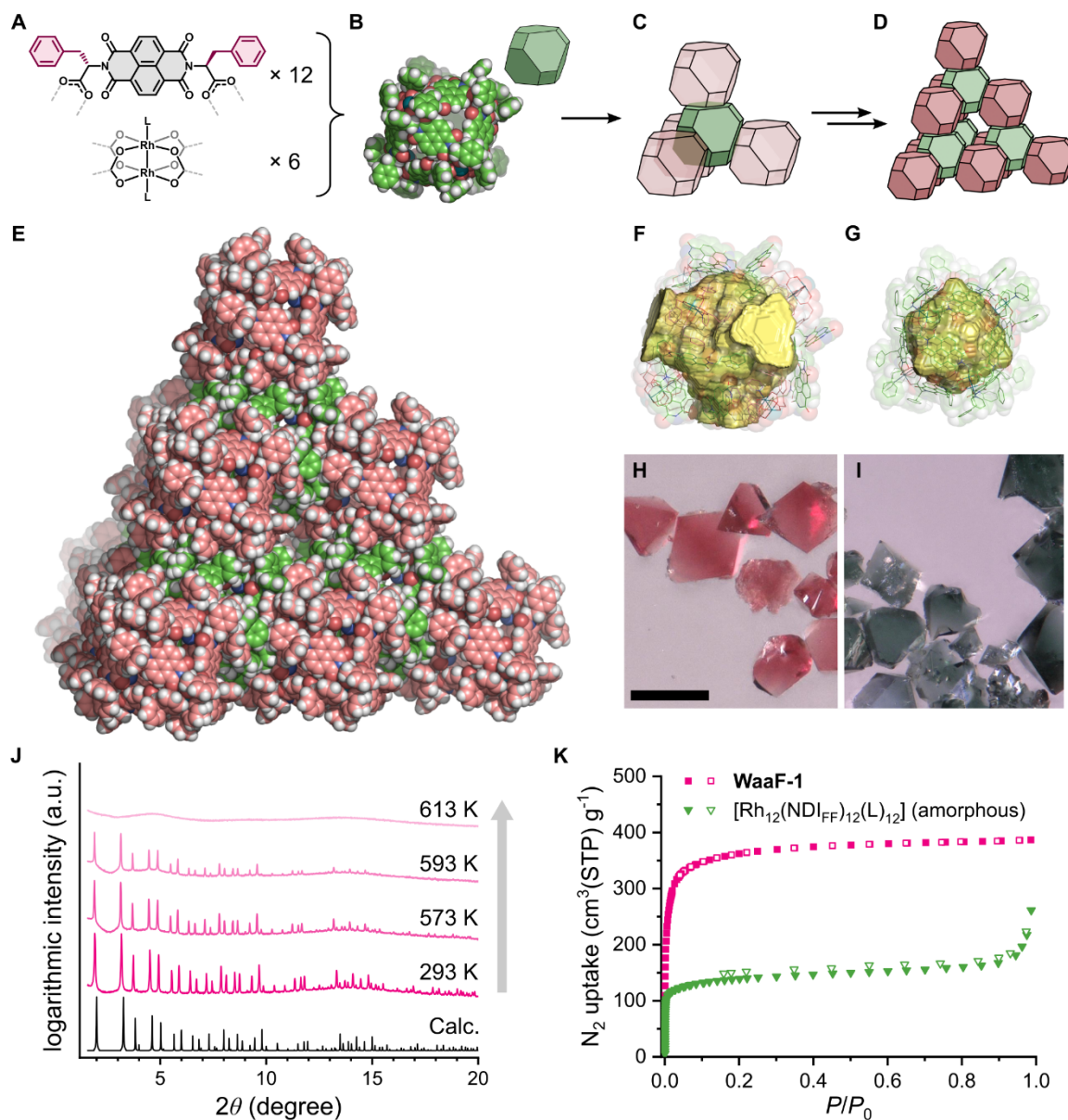


**Fig. 2: Supramolecular assembly of WaaF-1 and its stable open voids.** (A) chemical structure of  $\text{NDI}_{\text{FF}}$  ligand and dirhodium paddlewheel. (B) Crystal structure of supramolecular building block  $[\text{Rh}_{12}(\text{NDI}_{\text{FF}})_{12}(\text{L})_{12}]$  represented in a space-filling model. Solvent molecules coordinating on the dirhodium paddlewheels are abbreviated to clarify the molecular shape. (C, D) Schematic illustrations of (C) face-to-face stacking of octahedral

building blocks in the tetrahedral arrangement and (D) resulting formation of diamond-like network. (E) Crystal structure of **WaaF-1** in a space-filling model. Carbon atoms are shown in pink and green to clarify the boundary of MOP molecules. (F, G) Size comparison of (F) unit structure of the extended void in **WaaF-1** and (G) the intrinsic MOP cavity. (H, I) Optical microscopy images of **WaaF-1** single crystals in the absence of solvent, (H) before and (I) after the heating at 80 °C in the air (scale bar =100 μm). (J) VT-PXRD profiles of **WaaF-1** at elevating temperature in vacuum. Intensities were shown in a logarithmic scale. (K) Nitrogen gas sorption isotherms of **WaaF-1** (pink square) and [Rh<sub>12</sub>(NDI<sub>FF</sub>)<sub>12</sub>(L)<sub>12</sub>] before crystallization (green triangle) measured at 77 K. Filled and outlined symbols indicate adsorption and desorption, respectively.

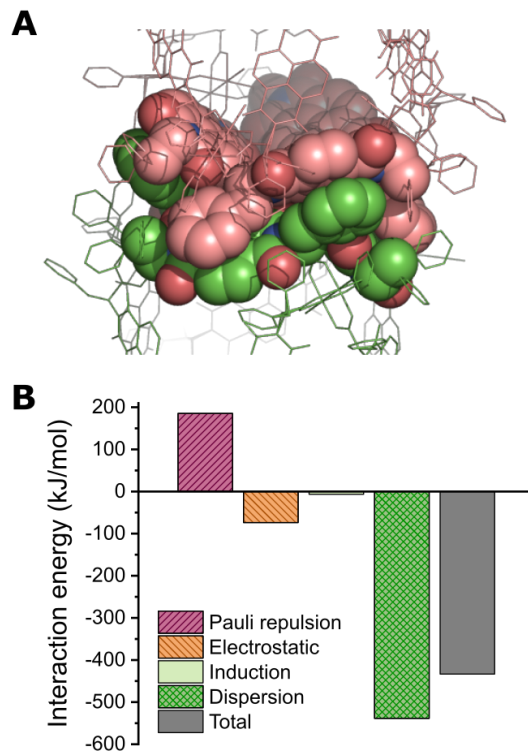


**Fig. 3: Strong van der Waals interactions in WaaF-1.** (A) Zoomed-up illustration of MOP-MOP contact in **WaaF-1**. Atoms not involving in the contact are shown in the wireframe representation for clarification. (B) EDA of MOP-MOP interaction in **WaaF-1** crystal structure. The calculation was performed at LRC- $\omega$ PBE/6-311G(d) levels of theory.

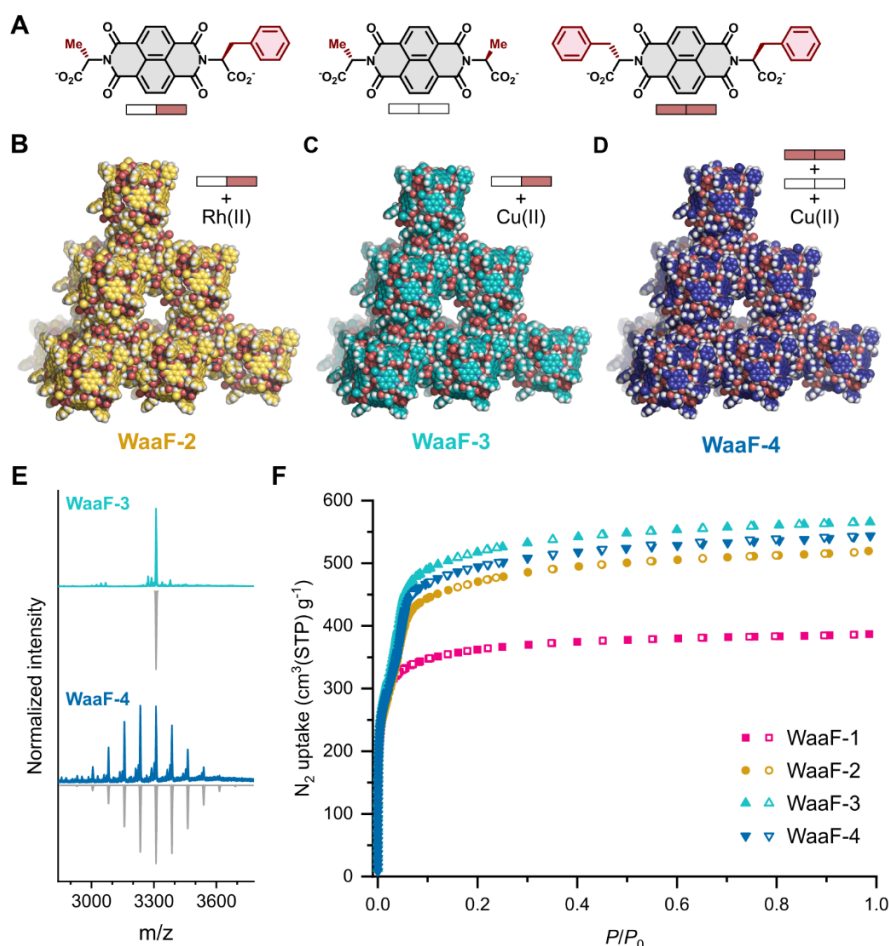


**Fig. 4: Assembly of WaaF-2, WaaF-3, and WaaF-4.** (A) Comparison of (left) NDI<sub>AF</sub>, (middle) NDI<sub>AA</sub>, and (right) NDI<sub>FF</sub> ligands. (B–D) Crystal structures of (B) **WaaF-2**, (C) **WaaF-3**, and (D) **WaaF-4** represented in a space-filling model. The NDI-based ligands and metal ions used in the synthesis are shown in the top-right. (E) Mass spectra of (top) **WaaF-3** and (bottom) **WaaF-4** measured after dissolving in chloroform/methanol mixed solvent. Simulated spectra for [M + 2Na]<sup>2+</sup> species are shown in grey below the observed spectra. (F) Nitrogen gas sorption isotherms of **WaaF-1** (pink square), **WaaF-2** (yellow circle), **WaaF-3** (light blue upward triangle), and **WaaF-4** (blue downward triangle) measured at 77 K. Filled and outlined symbols correspond to adsorption and desorption, respectively.

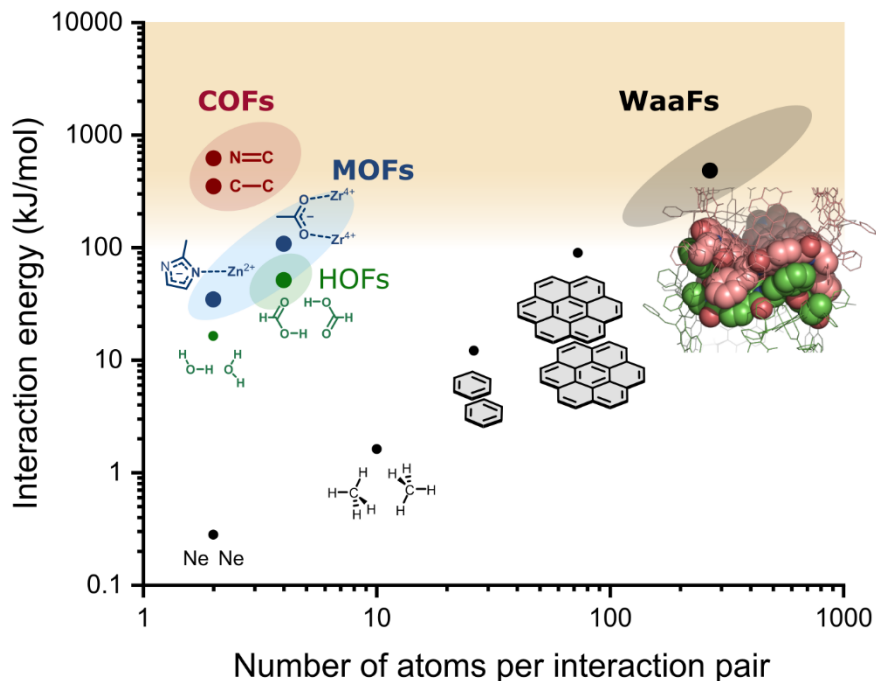


**Fig. 5: Strong bond in van der Waals frameworks.** Representative chemical bonds and intermolecular interactions are compared in terms of interaction energy and number of atoms involved in their interactions (6, 7, 31-35). The energy range higher than that of typical covalent bonds energy ( $>200$  kJ/mol) is filled in pale brown to indicate a possible criterion for “strong bond” required in open framework synthesis. Note that the interaction energy for **WaaF-1** is in this region. The trend in the plotted van der Waals interactions implies that strong van der Waals “bond” can be achieved by simply increasing the number of atoms in the intermolecular contact to more than 200.

## References

1. J. D. van der Waals, Over de Continuïteit van den Gas- en Vloeistofoestand. thesis, *University of Leiden* (1873).
2. F. Rouquerol, J. Rouquerol, K. S. W. Sing, P. Llewellyn, G. Maurin, in *Adsorption by Powders and Porous Solids*, (Academic Press, ed. 2, 2014), pp. 15–21.
3. G. S. Ratnaparkhi, R. Varadarajan, Thermodynamic and structural studies of cavity formation in proteins suggest that loss of packing interactions rather than the hydrophobic effect dominates the observed energetics. *Biochemistry* **39**, 12365–12374 (2000). doi: 10.1021/bi000775k
4. K. Autumn, M. Sitti, Y. A. Liang, A. M. Peattie, W. R. Hansen, S. Sponberg, T. W. Kenny, R. Fearing, J. N. Israelachvili, R. J. Full, Evidence for van der Waals adhesion in gecko setae. *Proc. Natl. Acad. Sci. U.S.A.* **99**, 12252–12256 (2002). doi: 10.1073/pnas.192252799
5. C. Gropp, S. Canossa, S. Wuttke, F. Gándara, Q. Li, L. Gagliardi, O. M. Yaghi, Standard Practices of Reticular Chemistry. *ACS Cent. Sci.* **6**, 1255–1273 (2020). doi: 10.1021/acscentsci.0c00592
6. E. M. Cabaleiro-Lago, J. Rodríguez-Otero, On the Nature of  $\sigma$ - $\sigma$ ,  $\sigma$ - $\pi$ , and  $\pi$ - $\pi$  Stacking in Extended Systems. *ACS Omega* **3**, 9348–9359 (2018). doi: 10.1021/acsomega.8b01339
7. J. K. Bristow, K. L. Svane, D. Tiana, J. M. Skelton, J. D. Gale, A. Walsh, Free Energy of Ligand Removal in the Metal-Organic Framework UiO-66. *J. Phys. Chem. C* **120**, 9276–9281 (2016). doi: 10.1021/acs.jpcc.6b01659
8. H. Heesch, F. Laves, Über dünne Kugelpackungen *Zeitschrift für Kristallographie - Crystalline Materials* **85**, 443–453 (1933). doi: 10.1524/zkri.1933.85.1.443
9. P. F. Damasceno, M. Engel, S. C. Glotzer, Predictive self-assembly of polyhedra into complex structures. *Science* **337**, 453–457 (2012). doi: 10.1126/science.1220869

10. S. Mollick, S. Mukherjee, D. Kim, Z. Qiao, A. V. Desai, R. Saha, Y. D. More, J. Jiang, M. S. Lah, S. K. Ghosh, Hydrophobic Shielding of Outer Surface: Enhancing the Chemical Stability of Metal-Organic Polyhedra. *Angew. Chem. Int. Ed.* **58**, 1041–1045 (2019). doi: 10.1002/anie.201811037
11. S. A. Boer, K. F. White, B. Slater, A. J. Emerson, G. P. Knowles, W. A. Donald, A. W. Thornton, B. P. Ladewig, T. D. M. Bell, M. R. Hill, A. L. Chaffee, B. F. Abrahams, D. R. Turner, A Multifunctional, Charge-Neutral, Chiral Octahedral M12 L12 Cage. *Chem. Euro. J.* **25**, 8489–8493 (2019). doi: 10.1002/chem.201901681
12. S. Furukawa, N. Horike, M. Kondo, Y. Hijikata, A. Carné-Sánchez, P. Larpent, N. Louvain, S. Diring, H. Sato, R. Matsuda, R. Kawano, S. Kitagawa, Rhodium-Organic Cuboctahedra as Porous Solids with Strong Binding Sites. *Inorg. Chem.* **55**, 10843–10846 (2016). doi: 10.1021/acs.inorgchem.6b02091
13. A. Nangia, G. R. Desiraju, Pseudopolymorphism: occurrences of hydrogen bonding organic solvents in molecular crystals. *Chem. Commun.*, 605–606 (1999). doi: 10.1039/A809755K
14. J. B. Maglic, R. Lavendomme, MoloVol: an easy-to-use program for analyzing cavities, volumes and surface areas of chemical structures. *J. Appl. Cryst.* **55**, 1033–1044 (2022). doi: 10.1107/S1600576722004988
15. J. W. M. Osterrieth, J. Rampersad, D. Madden, N. Rampal, L. Skoric, B. Connolly, M. D. Allendorf, V. Stavila, J. L. Snider, R. Ameloot, J. Marreiros, C. Ania, D. Azevedo, E. Vilarrasa-Garcia, B. F. Santos, X.-H. Bu, Z. Chang, H. Bunzen, N. R. Champness, S. L. Griffin, B. Chen, R.-B. Lin, B. Coasne, S. Cohen, J. C. Moreton, Y. J. Colón, L. Chen, R. Clowes, F.-X. Coudert, Y. Cui, B. Hou, D. M. D'Alessandro, P. W. Doheny, M. Dincă, C. Sun, C. Doonan, M. T. Huxley, J. D. Evans, P. Falcaro, R. Ricco, O. Farha, K. B. Idrees, T. Islamoglu, P. Feng, H. Yang, R. S. Forgan, D. Bara, S. Furukawa, E. Sanchez, J. Gascon, S. Telalović, S. K. Ghosh, S. Mukherjee, M. R. Hill, M. M. Sadiq, P. Horcajada, P. Salcedo-Abraira, K. Kaneko, R. Kukobat, J. Kevlin, S. Keskin, S. Kitagawa, K.-I. Otake, R. P. Lively, S. J. A. DeWitt, P. Llewellyn, B. V.

- Lotsch, S. T. Emmerling, A. M. Pütz, C. Martí-Gastaldo, N. M. Padial, J. García-Martínez, N. Linares, D. Maspoch, J. A. Suárez Del Pino, P. Moghadam, R. Oktavian, R. E. Morris, P. S. Wheatley, J. Navarro, C. Petit, D. Danaci, M. J. Rosseinsky, A. P. Katsoulidis, M. Schröder, X. Han, S. Yang, C. Serre, G. Mouchaham, D. S. Sholl, R. Thyagarajan, D. Siderius, R. Q. Snurr, R. B. Goncalves, S. Telfer, S. J. Lee, V. P. Ting, J. L. Rowlandson, T. Uemura, T. Iiyuka, M. A. van der Veen, D. Rega, V. Van Speybroeck, S. M. J. Rogge, A. Lemaire, K. S. Walton, L. W. Bingel, S. Wuttke, J. Andreato, O. Yaghi, B. Zhang, C. T. Yavuz, T. S. Nguyen, F. Zamora, C. Montoro, H. Zhou, A. Kirchon, D. Fairen-Jimenez, How Reproducible are Surface Areas Calculated from the BET Equation? *Adv. Mater.* **34**, e2201502 (2022). doi: 10.1002/adma.202201502
16. G. R. Lorz, A. J. Gosselin, B. A. Trump, A. H. P. York, A. Sturluson, C. A. Rowland, G. P. A. Yap, C. M. Brown, C. M. Simon, E. D. Bloch, Understanding Gas Storage in Cuboctahedral Porous Coordination Cages. *J. Am. Chem. Soc.* **141**, 12128–12138 (2019). doi: 10.1021/jacs.9b05872
17. L. D. Jacobson, J. M. Herbert, An efficient, fragment-based electronic structure method for molecular systems: self-consistent polarization with perturbative two-body exchange and dispersion. *J. Chem. Phys.* **134**, 094118 (2011). doi: 10.1063/1.3560026
18. J. M. Herbert, L. D. Jacobson, K. U. Lao, M. A. Rohrdanz, Rapid computation of intermolecular interactions in molecular and ionic clusters: self-consistent polarization plus symmetry-adapted perturbation theory. *Phys. Chem. Chem. Phys.* **14**, 7679–7699 (2012). doi: 10.1039/c2cp24060b
19. A. I. Kitaigorodskii, The principle of close packing and the condition of thermodynamic stability of organic crystals. *Acta Cryst.* **18**, 585–590 (1965). doi: 10.1107/S0365110X65001391
20. M. Mastalerz, Permanent porous materials from discrete organic molecules-towards ultra-high surface areas. *Chem. Euro. J.* **18**, 10082–10091 (2012). doi: 10.1002/chem.201201351

21. M. A. Little, A. I. Cooper, The chemistry of porous organic molecular materials. *Adv. Funct. Mater.* **30**, 1909842 (2020). doi: 10.1002/adfm.201909842
22. K. Sokołowski, W. Bury, I. Justyniak, D. Fairen-Jimenez, K. Sołtys, D. Prochowicz, S. Yang, M. Schröder, J. Lewiński, Permanent porosity derived from the self-assembly of highly luminescent molecular zinc carbonate nanoclusters. *Angew. Chem. Int. Ed.* **52**, 13414–13418 (2013). doi: 10.1002/anie.201306785
23. H. Yamagishi, H. Sato, A. Hori, Y. Sato, R. Matsuda, K. Kato, T. Aida, Self-assembly of lattices with high structural complexity from a geometrically simple molecule. *Science* **361**, 1242–1246 (2018). doi: 10.1126/science.aat6394
24. W. Bury, A. M. Walczak, M. K. Leszczyński, J. A. R. Navarro, Rational Design of Noncovalent Diamondoid Microporous Materials for Low-Energy Separation of C6-Hydrocarbons. *J. Am. Chem. Soc.* **140**, 15031–15037 (2018). doi: 10.1021/jacs.8b09522
25. S. Nakajima, K. Albrecht, S. Kushida, E. Nishibori, T. Kitao, T. Uemura, K. Yamamoto, U. H. F. Bunz, Y. Yamamoto, A fluorescent microporous crystalline dendrimer discriminates vapour molecules. *Chem. Commun.* **54**, 2534–2537 (2018). doi: 10.1039/c7cc09342j
26. C. G. Bezzu, L. A. Burt, C. J. McMonagle, S. A. Moggach, B. M. Kariuki, D. R. Allan, M. Warren, N. B. McKeown, Highly stable fullerene-based porous molecular crystals with open metal sites. *Nat. Mater.* **18**, 740–745 (2019). doi: 10.1038/s41563-019-0361-0
27. H. Yamagishi, M. Tsunoda, K. Iwai, K. Hengphasatporn, Y. Shigeta, H. Sato, Y. Yamamoto, Solvophobicity-directed assembly of microporous molecular crystals. *Commun. Chem.* **4**, 122 (2021). doi: 10.1038/s42004-021-00561-8
28. R. Banerjee, A. Phan, B. Wang, C. Knobler, H. Furukawa, M. O’Keeffe, O. M. Yaghi, High-throughput synthesis of zeolitic imidazolate frameworks and application to CO<sub>2</sub> capture. *Science* **319**, 939–943 (2008). doi: 10.1126/science.1152516

29. P. Li, N. A. Vermeulen, C. D. Malliakas, D. A. Gómez-Gualdrón, A. J. Howarth, B. L. Mehdi, A. Dohnalkova, N. D. Browning, M. O’Keeffe, O. K. Farha, Bottom-up construction of a superstructure in a porous uranium-organic crystal. *Science* **356**, 624–627 (2017). doi: 10.1126/science.aam7851
30. J. Li, D. F. Sava, V. Guillerm, T. Melliti, R. Luebke, J. F. Eubank, P. M. Bhatt, H. Jiang, M. Bonneau, Y. Belmabkhout, Z. Huang, A. Shkurenko, L. Wojtas, M. O’Keeffe, M. Eddaoudi, Using small building blocks to assemble ultra-complex, multifaceted metal-organic frameworks with zeolitic, mesoporous subnetwork. *Chem* (2023), doi: 10.1016/j.chempr.2023.09.026.
31. P. W. Atkins, T. L. Overton, J. P. Rourke, M. T. Weller, F. A. Armstrong, in *Shriver and Atkins’ Inorganic Chemistry* (Oxford University Press, ed. 5, 2010), pp. 59–61.
32. J. T. Hughes, T. D. Bennett, A. K. Cheetham, A. Navrotsky, Thermochemistry of Zeolitic Imidazolate Frameworks of Varying Porosity. *J. Am. Chem. Soc.* **135**, 598–601 (2013). doi: 10.1021/ja311237m
33. M. W. Feyereisen, D. Feller, D. A. Dixon, Hydrogen Bond Energy of the Water Dimer. *J. Phys. Chem.* **100**, 2993–2997 (1996). doi: 10.1021/jp9528601
34. T. Neuheuser, B. A. Hess, C. Reutel, E. Weber, Ab Initio Calculations of Supramolecular Recognition Modes. Cyclic versus Noncyclic Hydrogen Bonding in the Formic Acid/Formamide System. *J. Phys. Chem.* **98**, 6459–6467 (1994). doi: 10.1021/j100077a007
35. J. N. Israelachvili, in *Intermolecular and Surface Forces* (Academic Press, ed. 3, 2011), pp.109–111.

## METHODS

### Materials

Rhodium(III) chloride trihydrate was purchased from TANAKA Kikinzoku Kogyo K.K. 1,4,5,8-Naphthalenetetracarboxylic dianhydride, L-phenylalanine, and imidazole were purchased from Tokyo Chemical Industry. L-Alanine was purchased from Peptide Institute, Inc. Sodium acetate trihydrate, acetic acid, sodium carbonate was purchased from Nacalai Tesque, Inc. Spherical silica gel beads (63–219  $\mu\text{m}$ ) for the column chromatography were purchased from KANTO CHEMICAL Co., Inc. Other organic solvents/reagents were purchased from FUJIFILMS Wako Chemicals. All the chemicals were used as delivered.

### Synthesis

**Synthesis of dirhodium tetraacetate methanol adduct,  $[\text{Rh}_2(\text{OAc})_4(\text{MeOH})_2]$ .** Synthetic procedure was slightly modified from the reported method (36). Rhodium(III) chloride trihydrate 3.552 g (13.49 mmol, 1 eq.), sodium acetate trihydrate 7.126 g (52.37 mmol, 3.88 eq.), acetic acid 70 mL, and ethanol 70 mL were mixed in a 200 mL two-necked round-bottomed flask and this mixture was refluxed under argon atmosphere at 110 °C for two hours, where the green precipitate was formed upon reaction. The green precipitate was collected by suction filtration and dried in the air, yielding 4.541 g of the green crude product. This crude product was then placed in a 1 L round-bottomed flask with methanol 800 mL, and it was refluxed at 85 °C for 15 min until all solids were dissolved. This solution was filtered through paper while it was hot, and the small amount of solid product remained on the filter paper was redissolved in methanol 80 mL and filtered again. The combined product solution (ca. 880 mL) was reduced to around 400 mL using a rotary evaporator and then cooled in the freezer for five days to produce the product crystals. The precipitate was collected by suction filtration, washed with a small amount of ice-cold methanol, and dried in the air to yield dark green crystalline solid 2.788 g (5.51 mmol, 82% yield based on rhodium).

**Synthesis of H<sub>2</sub>NDI<sub>FF</sub>.** Synthesis was performed following the reported method with a modification of solvent used for the condensation reaction (10). 1,4,5,8-Naphthalenetetracarboxylic dianhydride 3.004 g (11.20 mmol, 1 eq.), L-phenylalanine 3.714 g (22.48 mmol, 2.01 eq.), and imidazole 13.2 g (194 mmol, 17.3 eq.) were mixed in a 100 mL round-bottomed flask and stirred at 110 °C for 1 hour until dark brown solution was obtained. After cooled down to around 90 °C, the solution was dissolved in water 100 mL, which was then acidified to pH 1-2 with concentrated hydrochloric acid to give a product precipitate. The precipitate was collected by suction filtration and thoroughly washed with water, followed by drying in vacuum at 50 °C overnight. Pale yellow solid 5.855 g was obtained (93% yield). <sup>1</sup>H NMR (DMSO-*d*<sub>6</sub>, 500 MHz) δ 8.65 (s, 2H), 7.17 (d, *J* = 6.8 Hz, 2H), 7.11 (t, *J* = 7.5 Hz, 4H), 7.04 (t, *J* = 7.3 Hz, 4H), 5.88 (dd, *J* = 9.4, 5.7 Hz, 2H), 3.62 (dd, *J* = 14.1, 5.6 Hz, 2H), 3.34 (dd, *J* = 14.1, 9.4 Hz, 2H).

**Synthesis of H<sub>2</sub>NDI<sub>AA</sub>.** Synthesis was performed following the reported method with a modification of solvent used for the condensation reaction (10). 1,4,5,8-Naphthalenetetracarboxylic dianhydride 5.003 g (18.65 mmol, 1 eq.), L-alanine 3.325 g (37.32 mmol, 2.00 eq.), and imidazole 20.0 g (294 mmol, 15.8 eq.) were mixed in a 100 mL round-bottomed flask and stirred at 110 °C for 1 hour until dark brown solution was obtained. After cooled down to around 90°C, the solution was dissolved in water 100 mL, which was then acidified to pH 1-2 with concentrated hydrochloric acid to give a product precipitate. The precipitate was collected by suction filtration and thoroughly washed with water, followed by drying in vacuum at 60 °C overnight. Pale brown solid 5.890 g was obtained (77% yield). <sup>1</sup>H NMR (DMSO-*d*<sub>6</sub>, 500 MHz) δ 12.84 (s, 2H), 8.72 (s, 2H), 5.61 (q, *J* = 6.9 Hz, 2H), 1.58 (d, *J* = 7.0 Hz, 6H).

**Synthesis of H<sub>2</sub>NDI<sub>AF</sub>.** 1,4,5,8-Naphthalenetetracarboxylic dianhydride 800 mg (2.98 mmol, 1 eq.), L-alanine 266 mg (2.98 mmol, 1 eq.), triethylamine 0.414 mL (2.98 mmol, 1 eq.), and DMF 18 mL were mixed in a sealed microwave reactor vessel and microwaved at 140 °C for 10 min to obtain pale brown solution. L-Phenylalanine 493 mg (2.98 mmol, 1 eq.) and triethylamine 0.414 mL (2.98 mmol, 1 eq.) were added to this mixture and further microwaved at 140 °C for 10 min to obtain dark brown solution. This process was separately

performed again, and ca. 40 mL of reaction mixture was obtained in total. The product was precipitated by adjusting pH to 1 with HCl aq. and by putting water 160 mL, from which brown sticky solid was precipitated. The clear supernatant was discarded, and the remained solid was further dispersed in dil. HCl aq. 200 mL. This solid was collected by suction filtration and washed with water. After drying in vacuum at 50 °C overnight, 2.095 g dark brown solid was obtained as the crude product. The target product was isolated by repeating silica gel column chromatography using toluene/ethyl acetate mixed-solvent eluent (ethyl acetate fraction was gradually increased from 5vol% to 70vol%) with 0.5 vol% of trifluoroacetic acid as additive. 350 mg of yellow solid was collected as a pure product (12% yield). <sup>1</sup>H NMR (DMSO-*d*<sub>6</sub>, 500 MHz) δ 13.03 (s, 2H), 8.68 (q, *J* = 7.6 Hz, 4H), 7.18 – 7.00 (m, 5H), 5.90 (dd, *J* = 9.7, 5.6 Hz, 1H), 5.59 (q, *J* = 7.0 Hz, 1H), 3.59 (dd, *J* = 14.1, 5.5 Hz, 1H), 3.35 (dd, *J* = 14.0, 9.7 Hz, 1H), 1.55 (d, *J* = 6.9 Hz, 3H). HRMS (ESI): [C<sub>26</sub>H<sub>18</sub>N<sub>2</sub>O<sub>8</sub> + Na]<sup>+</sup> actual; *m/z* 509.0957, calculated; *m/z* 509.0955, [C<sub>26</sub>H<sub>18</sub>N<sub>2</sub>O<sub>8</sub> - H]<sup>-</sup> actual; *m/z* 485.0995, calculated; *m/z* 485.0990.

**Synthesis of [Rh<sub>12</sub>(NDI<sub>FF</sub>)<sub>12</sub>(L)<sub>12</sub>].** [Rh<sub>2</sub>(OAc)<sub>4</sub>(MeOH)<sub>2</sub>] 501 mg (0.990 mmol, 1 eq.), H<sub>2</sub>NDI<sub>FF</sub> 1.397 g (2.483 mmol, 2.51 eq.), and *N,N*-dimethylacetamide (DMA) 50 mL were mixed in a 100 mL scintillation vial and it was sonicated for 1 min until homogeneously dispersed. Sodium carbonate 263 mg (2.48 mmol, 2.50 eq.) was added, and this mixture was heated in the preheated 120 °C oven for 15 hours, which yielded the mixture of dark green solution and brown solid. The green solution was isolated by a gravitational filtration through paper, and the product was precipitated by adding methanol 150 mL. The precipitate was collected by centrifugation (3600 rpm, 5 min), and washed with methanol 40 mL three times and with diethyl ether three times by repeating dispersion in a fresh solvent and collection by centrifugation. The collected precipitate was dried in vacuum at room temperature overnight. Pale green solid 640 mg was obtained (ca. 44% yield based on rhodium). <sup>1</sup>H NMR (CDCl<sub>3</sub>, 500 MHz) δ 8.65 (d, *J* = 7.6 Hz, 2H), 8.42 (d, *J* = 7.7 Hz, 2H), 7.25 – 7.09 (m, 10H), 6.18 (dd, *J* = 9.9, 5.6 Hz, 2H), 3.88 (dd, *J* = 14.2, 5.5 Hz, 2H), 3.28 (dd, *J* = 14.1, 9.9 Hz, 2H).

**Synthesis of WaaF-1.** Bulk powder sample of **WaaF-1** was obtained by the reprecipitation method to precisely control the solvent mixing ratio. 10 mg of  $[\text{Rh}_{12}(\text{NDI}_{\text{FF}})_{12}(\text{L})_{12}]$  was first dissolved in DMA 1.00 mL, and this green solution was added at once in the mixed solvent of ethanol 2.00 mL and pyridine 15  $\mu\text{L}$  at room temperature under vigorous stirring, from which a suspension of amorphous red solid was obtained. This suspension was kept undisturbed at 40 °C overnight to allow for crystallization. The colorless supernatant was discarded, and the red precipitate was washed with methanol 1 mL twice and then dried in the air at room temperature. Ca. 10 mg of red powder was obtained as a phase-pure **WaaF-1** bulk sample. Single crystals of **WaaF-1** suitable for SC-XRD measurements were prepared by the vapor diffusion method.  $[\text{Rh}_{12}(\text{NDI}_{\text{FF}})_{12}(\text{L})_{12}]$  2 mg dissolved in the mixture of DMA 100  $\mu\text{L}$  and pyridine 5  $\mu\text{L}$  was placed in a glass test tube, and this test tube was further sealed in a larger glass vial equipped with a few milliliters of ethanol. Single crystals of **WaaF-1** were harvested as red octahedral crystals formed on the wall of the test tube upon the slow diffusion of ethanol. Under this condition, red rhombic plate crystals with  $P2_12_12_1$  space group ( $[\text{Rh}_{12}(\text{NDI}_{\text{FF}})_{12}(\text{L})_{12}]$  molecular crystal with **fcu** packing topology) were also found to be formed on the bottom of the test tube as a pseudo-polymorph.

**Synthesis of WaaF-2.**  $[\text{Rh}_2(\text{OAc})_4(\text{MeOH})_2]$  80 mg (0.16 mmol, 1 eq.),  $\text{H}_2\text{NDI}_{\text{AF}}$  196 mg (0.403 mmol, 2.6 eq.), and *N,N*-dimethylacetamide (DMA) 8.00 mL were mixed in a 10 mL scintillation vial and it was sonicated for 1 min until homogeneously dispersed. Sodium carbonate 43 mg (0.40 mmol, 2.6 eq.) was added, and this mixture was heated in the preheated 100 °C oven for 37 hours, which yielded the mixture of dark green solution and brown solid. The green solution was isolated by filtration through paper, and the product was precipitated by adding methanol 42 mL. The precipitate was collected by centrifugation, and washed with methanol 20 mL three times and with diethyl ether 20 mL three times by repeating dispersion in a fresh solvent and collection by centrifugation. The collected precipitate was dried in the air overnight. Pale green solid 100 mg was obtained as amorphous  $[\text{Rh}_{12}(\text{NDI}_{\text{AF}})_{12}(\text{L})_{12}]$  (ca. 53% yield based on rhodium). Crystallization of  $[\text{Rh}_{12}(\text{NDI}_{\text{AF}})_{12}(\text{L})_{12}]$  into **WaaF-2** was achieved by the vapor diffusion of ethanol into DMA

solution of  $[\text{Rh}_{12}(\text{NDI}_{\text{AF}})_{12}(\text{L})_{12}]$ , which yielded green octahedral crystals as a phase-pure material. This crystalline solid was repeatedly washed with methanol and kept under methanol until it was delivered for the characterizations.

**Synthesis of WaaF-3.** 0.10 M solutions of  $\text{H}_2\text{NDI}_{\text{AF}}$  and copper(II) nitrate trihydrate were separately prepared in DMF, and 2 mL of the two solution were mixed in a 10 mL scintillation vial. Ethanol 4.00 mL was added to this solution, and the mixture was heated at 80 °C for 20 hours. Blue octahedral crystals were formed upon heating as a phase-pure crystalline material of **WaaF-3** (ca. 50% yield). This crystalline solid was repeatedly washed with methanol and kept under methanol until it was delivered for the characterizations.

**Synthesis of WaaF-4.** 0.10 M solutions of  $\text{H}_2\text{NDI}_{\text{AA}}$ ,  $\text{H}_2\text{NDI}_{\text{FF}}$  and copper(II) nitrate trihydrate were separately prepared in DMF. 1 mL of the  $\text{H}_2\text{NDI}_{\text{AA}}$  and  $\text{H}_2\text{NDI}_{\text{FF}}$  solutions were mixed with 2 mL of copper nitrate solution in a 20 mL scintillation vial, and ethanol 4.00 mL was added. Upon the heating at 80 °C for 20 hours, blue octahedral crystals were formed as a phase-pure crystalline material of **WaaF-4** (ca. 50% yield). This crystalline solid was repeatedly washed with methanol and kept under methanol until it was delivered for the characterizations.

## Instrumentation and characterization

**Nuclear Magnetic Resonance.** All  $^1\text{H}$ -nuclear magnetic resonance (NMR) spectra were recorded at ambient temperature (ca. 25 °C) on the Avance III 500 spectroscope (Bruker) equipped with 24-specimen automatic sample loader, and data analysis was done by MestReNova version 14.2.3-29241. Measurement specimens of  $\text{H}_2\text{NDI}_{\text{FF}}$ ,  $\text{H}_2\text{NDI}_{\text{AA}}$ , and  $\text{H}_2\text{NDI}_{\text{AF}}$  were prepared by dissolving a few milligrams of solid samples in  $\text{DMSO-}d_6$  solvent 0.600 mL and directly delivered for the measurement. However,  $[\text{Rh}_{12}(\text{NDI}_{\text{FF}})_{12}(\text{L})_{12}]$  was found to be not soluble in pure  $\text{CDCl}_3$  and a few microliters of methanol had to be added to help the dissolution. For the identification of ligand mixing ratio in **WaaF-4**, dried sample of **WaaF-4** was acid-digested by deuterated hydrochloric acid (DCl) 50  $\mu\text{L}$  mixed with  $\text{DMSO-}d_6$  0.600 mL (Fig. S12).

**Infrared Spectroscopy.** To characterize the coordination bonds in the series of WaaFs, Fourier transform infrared spectroscopy (FT-IR) data were recorded in vacuum at ambient temperature with the FT/IR-6100 spectroscope (JASCO) in the attenuated total reflection (ATR) mode with accumulation of 128 scans (Fig. S20). All specimens were prepared in the same conditions of evaporation of methanol solvent at ambient temperature in vacuo and following heated evacuation at 100 °C overnight.

**Mass Spectrometry.** To fully characterize the newly synthesized H<sub>2</sub>NDI<sub>AF</sub> ligand, Electrospray ionization mass spectrometry (ESI-MS) was performed on the Exactive Plus spectrometer (Thermo Fischer Scientific). Both positive and negative modes provided consistent m/z signals in the high-resolution measurements. Cryospray ionization mass spectrometry (CSI-MS) on the micrOTOF II spectrometer (Bruker Daltonics) was adopted for the characterization of **WaaF-3** and **WaaF-4** to avoid the decomposition of MOP molecules in the ionization process. Dried solid samples of **WaaF-3** and **WaaF-4** were dissolved in the mixed solvent of chloroform/methanol (95:5 volume ratio) and delivered for the MS measurements. Only positive mode measurement provided clear m/z signals corresponding to the target species for both samples (Fig. S13, S14). Isotopic patterns of each expected species were simulated by the web-based enviPat program (<https://www.envipat.eawag.ch/>) (37), and the relative abundance of each isomer in **WaaF-4** was simulated by assuming statistical (random) scrambling of the NDI<sub>AA</sub> and NDI<sub>FF</sub> ligands in the octahedral MOP scaffold.

**Thermogravimetric Analysis.** Thermal stability of the materials was studied by thermogravimetric analysis (TGA) recorded on the Thermo plus EVO2 instrument (Rigaku) equipped with the automatic sample loader (Fig. S4A, S19). A few milligrams of solid samples were placed in an aluminum pan and the sample weight was recorded in the temperature scan from 30 °C to 500 °C at 5 °C/min under nitrogen gas flow.

**Field Emission Scanning Electron Microscopy.** Micrographs of microcrystalline samples were captured by field emission scanning electron microscope (FE-SEM) technique, performed on the SU5000 microscope (Hitachi). Solid samples wet with organic solvents

were drop-casted on a copper-based conductive tape substrate and dried in vacuo at ambient temperature before delivered for the imaging.

**Ultraviolet-Visible Absorption Spectroscopy** Ultraviolet-visible (UV-Vis) absorption spectra of **WaaF-1** powder sample was recorded on the V-670 spectroscope (JASCO) equipped with an integration sphere. Alumina powder was used to record the baseline spectrum. To control the gas environment around the powder sample during the measurement, the chamber-shaped lab-made sample holder was designed and 3D-printed with PLA plastic using the Finder2 3D printer (FLASHFORGE). Powder sample suspended in methanol was drop-casted and dried on a  $20 \times 20 \text{ mm}^2$  glass plate, and this plate was fixed in the sample holder so that the sample side directed to the “chamber” part of the holder and the glass side directed to the integration sphere window. Two rubber tubes were connected to the sample holder, and specific gas was flowed to the chamber from one of the rubber tube and the other tube was used to exhaust the gas from the chamber. Absorption spectra was recorded as a diffuse reflection from the glass window of the sample holder under continuous gas flow.

**Gas Sorption** Prior to gas sorption experiments, powder samples of  $[\text{Rh}_{12}(\text{NDI}_{\text{AF}})_{12}(\text{L})_{12}]$  (including as-synthesized amorphous building blocks, **WaaF-1**, and its **fcu**-packed polymorph) were activated by heating at  $100 \text{ }^\circ\text{C}$  for 12 hours under vacuum. In the case of the other materials (**WaaF-2**, **WaaF-3**, and **WaaF-4**), methanol-wet crystals were first desolvated in mild condition by the super-critical  $\text{CO}_2$  drying process carried out on SCLEAD-2BD autoclave (KISCO) using super-critical  $\text{CO}_2$  at 14 MPa and  $50 \text{ }^\circ\text{C}$  for 2 h to keep crystallinity as much as possible. Then, the desolvated samples were activated by heating at  $100 \text{ }^\circ\text{C}$  for 12 hours under vacuum. Note that this two-step activation is not necessary for **WaaF-1**, which showed almost the same gas uptake regardless of super-critical  $\text{CO}_2$  drying process. Gas sorption experiments were performed on the volumetric gas sorption apparatus BELSORP MINI X (MicrotracBEL Corp.) (Fig. 2K, 4F, S21). In the nitrogen gas sorption experiments, sample tube temperature was maintained at 77 K by using a Dewar vessel equipped with liquid nitrogen. For the carbon dioxide gas sorption experiments, sample tube temperature was maintained at 195 K by the mixture of crashed dry ice and isopropyl alcohol. All the carbon dioxide gas sorption experiments were performed just after

the nitrogen gas sorption experiments without exchanging samples. For the calculation of Brunauer-Emmett-Teller surface area from nitrogen gas adsorption isotherms by BETSI program (15), input data for the program was prepared by manually edit the isotherm; data points showing decreasing  $P/P_0$  or decreasing gas uptake from last data point were removed from the isotherm data. This data curation was found to be inevitable to run the BETSI program, as the program can only process monotonically increasing isotherms. The results of analysis performed by BETSI are shown in Fig. S7, S23–S25.

**Powder X-ray Diffraction.** Powder X-ray diffraction (PXRD) profiles of **fcu**-packed  $[\text{Rh}_{12}(\text{NDI}_{\text{AF}})_{12}(\text{L})_{12}]$  and water-treated **WaaF-1** were recorded on a SmartLab diffractometer (Rigaku) with Cu  $K\alpha$  radiation ( $\lambda = 1.54056 \text{ \AA}$ ) and D/teX Ultra one-dimensional detector arranged in Bragg-Brentano geometry (Fig. S2, S28B). Variable temperature PXRD (VT-PXRD) profiles of **WaaF-1** and the other PXRD profiles of **WaaF-1**, **2**, **3**, and **4** are measured in BL02B2 beamline in SPring-8, Japan (Fig. S4B, S15, S16). Powder samples were placed in glass capillaries and kept rotated during data collection. Diffractogram was recorded with synchrotron radiation ( $\lambda = 0.9993 \text{ \AA}$ ) on a one-dimensional semiconductor detector arranged in transmission mode. Measurements were conducted at 25 °C otherwise noted. Sample temperature was controlled by continuous flow of nitrogen gas on the sample position. Gas atmosphere was kept under dynamic vacuum for dried samples. Le Bail fitting of the observed diffractograms was performed on Jana2006 software (39).

**Single Crystal X-ray Diffraction.** Single crystal X-ray diffraction (SC-XRD) experiments for **WaaF-1** and its **fcu**-packed polymorph, solvent-wet **WaaF-3** and **4** were performed in BL02B1 beamline in SPring-8. For the data collection for desolvated **WaaF-1**, solvent-wet single crystals were left in the air to evaporate the solvent and further heated in the 80 °C oven to complete solvent removal. The dried single crystal was fixed on the tip of polyimide loop by the help of silicone grease and delivered for the measurement. For the rest of samples, solvent-wet single crystals were briefly washed in viscose oil (Cargille Immersion Oil Type NVH) to remove excess solvent from the crystal surface and quickly cooled to ca. 100 K by cryogenic nitrogen gas flow on the goniometer. All diffraction experiments were performed at 100 K with the synchrotron radiation ( $\lambda = 0.4136 \text{ \AA}$  or  $0.4128 \text{ \AA}$ ) and a PILATUS3 X

CdTe 1M (DECTRIS) detector. SC-XRD experiments for **WaaF-2** single crystal was performed in high-flux BL40XU beamline in SPring-8. Single crystal of solvent-wet **WaaF-2** was fixed on the tip of polyimide loop using viscose oil (Cargille Immersion Oil Type NVH) and diffraction experiment was performed at 100 K with the synchrotron radiation ( $\lambda = 0.8097 \text{ \AA}$ ) in the microbeam focusing mode and with an EIGER X 1M (DECTRIS) detector. SC-XRD experiments for desolvated **WaaF-3** and **4** single crystals were performed with XtaLAB P200 diffractometer (Rigaku) equipped with a MicroMax-007 HF X-ray generator and a PILATUS 200K detector. Single crystal samples of desolvated **WaaF-3** and **4** were prepared by the super-critical CO<sub>2</sub> drying process and following heating at ca. 100 °C under vacuum. The surface of these dried single crystals were quickly coated with silicone grease to prevent moisture and immediately delivered for the diffraction measurements. Data collection was conducted at -95 °C under cryogenic nitrogen gas flow.

Unit cell determination, diffraction intensity integration, and empirical absorption collection were processed on the CrysAlisPro ver. 41.93a software. Structure solution by intrinsic phasing was calculated by SHELXT program (40) via graphic user interface of Olex2 ver. 1.5. Structure refinement by least square method (L.S.) was performed by SHELXL program (41). Exceptionally, refinement of **fcu**-packed [Rh<sub>12</sub>(NDI<sub>FF</sub>)<sub>12</sub>(L)<sub>12</sub>] crystal structure was mostly done by conjugated gradient least square method (CGLS) to perform refinement cycles in a reasonable calculation time and finally refined by L.S. method. In addition to structural analysis, diffraction images were also assessed by reciprocal reconstruction calculated by CrysAlisPro to confirm the crystallinity and absence of twin (Fig. S6A, S17A, S18A).

All atoms were anisotropically modeled except severely disordered atoms (Fig. S6B, S10, S17B, S18B). All the phenyl groups originating from phenylalanine residues were constrained to regular hexagonal geometries by AFIX66. To model chemically sound bond distances, SADI was mainly applied to restrain interatomic distance and angles, but DFIX was also utilized when there is no chemically identical bonds to be restrained together. FLAT was also applied when SADI and DFIX does not improve unnatural distortion of approximately flat structures. SIMU or RIGU was applied to constrain displacement

parameters to physically sound values, and ISOR was also applied when SIMU or RIGU was found to be not enough for restraining the parameter. When residual electron density showed clear positional disorder of functional groups at multiple sites, corresponding atomic occupancies for each position were fined to become unity in total. Here, when two C atoms locating at the same position (e.g., methyl group and benzyl group's methylene group) can be refined as a superposition of two atoms (i.e., when two different types of H atoms can be modeled), EXYZ and EADP were applied to the overlapping C atoms. After refining non-H atoms, H atoms were modeled by riding onto C atoms with fixed C-H bond distances and fixed H-C-H angles. Finally, electron density from disordered solvent molecules were implicitly modeled by the "Mask" of Olex2 (as known as SQUEEZE in PLATON program). Note that this Mask processing was not applied to the desolvated **WaaF-3** and **4** because these samples did not show solvent electron density in the refinement, which is consistent to the sample preparation procedures.

All crystallographic data is deposited in

**Density Functional Theory Calculations.** Density functional theory (DFT) calculations were performed with Q-Chem ver. 6.0.0 software (42), calculated on the SuperComputer System of Institute for Chemical Research, Kyoto University.

UV-Vis spectra of dirhodium(II) paddlewheels were simulated based on the time-dependent DFT (TDDFT) calculations. Because TDDFT calculation on the whole MOP structure is computationally too expensive, dirhodium tetraacetate, which is a major chromophore of the MOP in the visible light region, was selected as model. Two kinds of pyridine/water adduct,  $[\text{Rh}_2(\text{OAc})_4(\text{pyridine})]$  and  $[\text{Rh}_2(\text{OAc})_4(\text{pyridine})(\text{H}_2\text{O})]$ , were modeled as the most plausible coordination states of dirhodium(II) paddlewheels in **WaaF-1** and they were geometrically optimized at the B3LYP/6-31G (for C, N, O, H) and LANL2DZ (for Rh) levels of theory. Then, 12 excited states and corresponding oscillator strengths were calculated at the TD-B3LYP/6-311G(d) (C, N, O, H) and LANL2DZ (Rh) levels of theory. For the simulation of broadened absorption spectra, Gaussian distribution of absorption energy was assumed and corresponding Gaussian curves were calculated based on the calculated 12 pairs of excitation

energy and oscillator strength using a python program written by the author (ST). Finally, simulated absorption spectra were plotted by wavelength (Fig. S5A).

Energy decomposition analysis (EDA) of MOP-MOP interaction was performed based on the explicit polarization + symmetry-adapted perturbation theory (XSAPT) method, which can calculate large-scale model structures more efficiently than the other EDA methods (17, 18). However, because the whole MOP pair structure is still computationally too expensive as EDA calculation model, we clipped out a partial structure of MOP-MOP molecular contact by a careful inspection of desolvated **WaaF-1** crystal structure. Six NDI<sub>FF</sub> ligands apart from carboxylate groups were firstly identified as major part of MOP-MOP contact and the rest of atoms were deleted from the model. Then, the six out of twelve phenyl groups of phenylalanine residues were also removed from the model as they are crystallographically disordered and not explicitly involving in the intermolecular contact. 18 Hydrogen atoms were added to the “bond cleaved” positions on carbon atoms to generate a chemically sound molecular. As a result these modeling process, a pair of N-substituted NDI molecule trimer (288 atoms in total) was obtained as a minimum model structure for the MOP-MOP contact. XSAPT calculation was performed with this structure by taking a trimer as one fragment and interaction between the two trimer was evaluated at the LRC- $\omega$ PBE/6-311G(d) levels of theory, where many-body dispersion (MBD) method was adopted for a dispersion correction (43).

In the model structure of **WaaF-1** described above, there are six pairs of NDI-benzyl stacking structure. For the estimation of MOP-MOP interaction energy in **WaaF-2**, which is similar but estimated to have less number of NDI-phenyl pairs from **WaaF-1**, the model structure for **WaaF-2** MOP-MOP contact was generated by cutting different number of phenyl groups from the **WaaF-1** model structure (Fig. S11B). When phenyl group(s) was removed from the model, hydrogen atom(s) was added to the bond-cleaved carbon atom(s). XSAPT+MBD calculations were performed at the same levels of theory for each model, and the calculated interaction energy was plotted against the number of NDI-benzyl stacking pairs (Fig. S11C).

## References

36. P. Legzdins, R. W. Mitchell, G. L. Rempel, J. D. Ruddick, G. Wilkinson, The protonation of ruthenium- and rhodium-bridged carboxylates and their use as homogeneous hydrogenation catalysts for unsaturated substances. *J. Chem. Soc. A*, 3322–3326 (1970). doi: 10.1039/J19700003322
37. M. Loos, C. Gerber, F. Corona, J. Hollender, H. Singer, Accelerated isotope fine structure calculation using pruned transition trees. *Anal. Chem.* **87**, 5738–5744 (2015). doi: 10.1021/acs.analchem.5b00941
38. J. D. Evans, V. Bon, I. Senkovska, S. Kaskel, A Universal Standard Archive File for Adsorption Data. *Langmuir* **37**, 4222–4226 (2021). doi: 10.1021/acs.langmuir.1c00122
39. V. Petříček, M. Dušek, L. Palatinus, Crystallographic Computing System JANA2006: General features. *Zeitschrift für Kristallographie - Crystalline Materials* **229**, 345–352 (2014). doi: 10.1515/zkri-2014-1737
40. G. M. Sheldrick, SHELXT - integrated space-group and crystal-structure determination. *Acta Cryst.* **A71**, 3–8 (2015). doi: 10.1107/S2053273314026370
41. G. M. Sheldrick, Crystal structure refinement with SHELXL. *Acta Cryst.* **B71**, 3–8 (2015). doi: 10.1107/S2053229614024218
42. E. Epifanovsky, A. T. B. Gilbert, X. Feng, J. Lee, Y. Mao, N. Mardirossian, P. Pokhilko, A. F. White, M. P. Coons, A. L. Dempwolff, Z. Gan, D. Hait, P. R. Horn, L. D. Jacobson, I. Kaliman, J. Kussmann, A. W. Lange, K. U. Lao, D. S. Levine, J. Liu, S. C. McKenzie, A. F. Morrison, K. D. Nanda, F. Plasser, D. R. Rehn, M. L. Vidal, Z.-Q. You, Y. Zhu, B. Alam, B. J. Albrecht, A. Aldossary, E. Alguire, J. H. Andersen, V. Athavale, D. Barton, K. Begam, A. Behn, N. Bellonzi, Y. A. Bernard, E. J. Berquist, H. G. A. Burton, A. Carreras, K. Carter-Fenk, R. Chakraborty, A. D. Chien, K. D. Closser, V. Cofer-Shabica, S. Dasgupta, M. de Wergifosse, J. Deng, M. Diedenhofen, H. Do, S. Ehlert, P.-T. Fang, S. Fatehi, Q. Feng, T. Friedhoff, J. Gayvert, Q. Ge, G. Gidofalvi, M. Goldey, J. Gomes, C. E. González-Espinoza, S. Gulania, A. O. Gunina, M. W. D. Hanson-Heine, P. H. P. Harbach, A. Hauser, M. F. Herbst, M. Hernández Vera, M.

Hodecker, Z. C. Holden, S. Houck, X. Huang, K. Hui, B. C. Huynh, M. Ivanov, Á. Jász, H. Ji, H. Jiang, B. Kaduk, S. Kähler, K. Khistyayev, J. Kim, G. Kis, P. Klunzinger, Z. Koczor-Benda, J. H. Koh, D. Kosenkov, L. Koulias, T. Kowalczyk, C. M. Krauter, K. Kue, A. Kunitsa, T. Kus, I. Ladjánszki, A. Landau, K. V. Lawler, D. Lefrancois, S. Lehtola, R. R. Li, Y.-P. Li, J. Liang, M. Liebenthal, H.-H. Lin, Y.-S. Lin, F. Liu, K.-Y. Liu, M. Loipersberger, A. Luenser, A. Manjanath, P. Manohar, E. Mansoor, S. F. Manzer, S.-P. Mao, A. V. Marenich, T. Markovich, S. Mason, S. A. Maurer, P. F. McLaughlin, M. F. S. J. Menger, J.-M. Mewes, S. A. Mewes, P. Morgante, J. W. Mullinax, K. J. Oosterbaan, G. Paran, A. C. Paul, S. K. Paul, F. Pavošević, Z. Pei, S. Prager, E. I. Proynov, Á. Rák, E. Ramos-Cordoba, B. Rana, A. E. Rask, A. Rettig, R. M. Richard, F. Rob, E. Rossomme, T. Scheele, M. Scheurer, M. Schneider, N. Sergueev, S. M. Sharada, W. Skomorowski, D. W. Small, C. J. Stein, Y.-C. Su, E. J. Sundstrom, Z. Tao, J. Thirman, G. J. Tornai, T. Tsuchimochi, N. M. Tubman, S. P. Veccham, O. Vydrov, J. Wenzel, J. Witte, A. Yamada, K. Yao, S. Yeganeh, S. R. Yost, A. Zech, I. Y. Zhang, X. Zhang, Y. Zhang, D. Zuev, A. Aspuru-Guzik, A. T. Bell, N. A. Besley, K. B. Bravaya, B. R. Brooks, D. Casanova, J.-D. Chai, S. Coriani, C. J. Cramer, G. Cserey, A. E. DePrince 3rd, R. A. DiStasio Jr, A. Dreuw, B. D. Dunietz, T. R. Furlani, W. A. Goddard 3rd, S. Hammes-Schiffer, T. Head-Gordon, W. J. Hehre, C.-P. Hsu, T.-C. Jagau, Y. Jung, A. Klamt, J. Kong, D. S. Lambrecht, W. Liang, N. J. Mayhall, C. W. McCurdy, J. B. Neaton, C. Ochsenfeld, J. A. Parkhill, R. Peverati, V. A. Rassolov, Y. Shao, L. V. Slipchenko, T. Stauch, R. P. Steele, J. E. Subotnik, A. J. W. Thom, A. Tkatchenko, D. G. Truhlar, T. Van Voorhis, T. A. Wesolowski, K. B. Whaley, H. L. Woodcock 3rd, P. M. Zimmerman, S. Faraji, P. M. W. Gill, M. Head-Gordon, J. M. Herbert, A. I. Krylov, Software for the frontiers of quantum chemistry: An overview of developments in the Q-Chem 5 package. *J. Chem. Phys.* **155**, 084801 (2021). doi: 10.1063/5.0055522

43. K. Carter-Fenk, K. U. Lao, K.-Y. Liu, J. M. Herbert, Accurate and Efficient ab Initio Calculations for Supramolecular Complexes: Symmetry-Adapted Perturbation Theory

- with Many-Body Dispersion. *J. Phys. Chem. Lett.* **10**, 2706–2714 (2019). doi: 10.1021/acs.jpcclett.9b01156
44. P. R. Spackman, M. J. Turner, J. J. McKinnon, S. K. Wolff, D. J. Grimwood, D. Jayatilaka, M. A. Spackman, CrystalExplorer: a program for Hirshfeld surface analysis, visualization and quantitative analysis of molecular crystals. *J. Appl. Cryst.* **54**, 1006–1011 (2021). doi: 10.1107/S1600576721002910
45. Hansen C. M. in *Hansen Solubility Parameters: A User's Handbook* (CRC Press, ed. 2, 2007). pp. 345–483

## **Acknowledgments**

The authors acknowledge Prof. Kuniyoshi Sugimoto (Kindai University) for the generous support on synchrotron SC-XRD measurements and Prof. Daniel M. Packwood (Kyoto University) for a fruitful discussion on DFT calculations. The authors thank the iCeMS Analysis Centre for access to analytical instruments. The synchrotron radiation experiments of SC-XRD and PXRD were performed at the BL02B1, BL02B2, and BL40XU of SPring-8 with the approval of the Japan Synchrotron Radiation Research Institute (JASRI) (Proposal No. 2022B0512, 2022B1624, 2023A1747, 2023B1860, 2023B1307, 2022B1623, 2023B1631). Computation time for DFT calculations was provided by the SuperComputer System, Institute for Chemical Research, Kyoto University. This work was supported by The Japan Science Society for the Sasakawa Research Grant (2023-3034) for S. T. and JSPS KAKENHI grant number 23H00298 (Kiban A) and MEXT Program: Data Creation and Utilization-Type Material Research and Development (Project Grant Number JPMXP1122714694) for S. F.

## **Author contributions**

S.F. and S.T. conceived the project and directed the research. S.T. performed all experiments and calculations. S.T. and S.F. analyzed the data and wrote the manuscript. All authors discussed the results and commented on the manuscript.

## **Competing Financial Interests:**

The authors declare that they have no competing financial interests.

## **Supplementary information**

Extended data are included in the supplementary information file.